ADVANCED PHYSICS RESEARCH Open Access
www.advphysicsres.com

Berry Curvature Induced Valley Hall Effect in Non-Encapsulated hBN/Bilayer Graphene Heterostructure Aligned with Near-Zero Twist Angle

Teppei Shintaku, Afsal Kareekunnan, Masashi Akabori, Kenji Watanabe, Takashi Taniguchi, and Hiroshi Mizuta*

Valley Hall effect is observed in asymmetric single-layer and bilayer graphene systems. In single-layer graphene systems, asymmetry is introduced by aligning graphene with hexagonal boron nitride (hBN) with a near-zero twist angle, breaking the sub-lattice symmetry. Although a similar approach is used in bilayer graphene to break the layer symmetry and thereby observe the valley Hall effect, the bilayer graphene is sandwiched with hBN on both sides in those studies. This study looks at a much simpler, non-encapsulated structure where hBN is present only at the top of graphene. The crystallographic axes of both hBN and bilayer graphene are aligned. A clear signature of the valley Hall effect through non-local resistance measurement (R_{NL}) is observed. The observed non-local resistance can be manipulated by applying a displacement field across the heterostructure. Furthermore, the electronic band structure and Berry curvature calculations validate the experimental observations.

1. Introduction

With the introduction of 2D materials, the valley degree of freedom of carriers has gained much prominence in recent years.[1–3] Materials like graphene and MoS_2 have two in-equivalent valleys at the K and K′ high symmetry points of their Brillouin zone, which can be interpreted as valley-up and valley-down, much like the spin degree of freedom of carriers. However, the fundamental criterion for a material to be valleytronic is to have a broken inversion symmetry. While single-layer graphene is symmetric, aligning graphene with hexagonal boron nitride (hBN) with a near-zero twist angle has proven to break the sub-lattice symmetry of the graphene layer.[4–7] Such a system has exhibited the valley Hall effect (VHE) due to the emergence of Berry curvature at the valley as a result of broken inversion symmetry.[8–10] As for bilayer graphene, the asymmetry can be introduced by either applying an out-of-plane electric field across the layers or by aligning with an hBN layer, both of which break the layer symmetry of the system as they introduce different potentials between the top and bottom layers of the bilayer.[11–15] Both methods have been employed to observe VHE in bilayer graphene in recent years.[16–19]

In the case of single-layer graphene, it has been shown that both encapsulated and non-encapsulated graphene exhibit the valley Hall effect, provided either of the hBN (top or bottom) is oriented with graphene.[8] As for bilayer graphene, the valley Hall effect is observed by hBN alignment only in encapsulated systems.[18,19] Here, hBN is present at the top and bottom of the bilayer graphene with one of the hBN aligned and the other misaligned by more than 10° to avoid the formation of a double moiré pattern. However, it has been shown theoretically that aligning hBN with bilayer graphene in a non-encapsulated configuration can also break the symmetry of the system and induce Berry curvature.[20] Considering the complexity in fabricating an encapsulated heterostructure, in this study, we explore the VHE in non-encapsulated hBN/bilayer graphene heterostructure (hBN/bilayer graphene/SiO_2) with the hBN aligned with the bilayer graphene. We observed a strong VHE signal at the primary Dirac point through non-local electrical measurement. The VHE signal could be further manipulated by applying a displacement electric field across the layers. We also performed ab initio calculations, which show that aligned hBN/bilayer graphene heterostructure has an intrinsic bandgap and a non-zero Berry curvature. The bandgap and the Berry curvature can be manipulated with an out-of-plane electric field applied across the layers.

2. Results and Discussion

The hBN/bilayer graphene heterostructure is fabricated following the dry transfer method.[21] Two devices, denoted as Device A

T. Shintaku, A. Kareekunnan, M. Akabori, H. Mizuta
Japan Advanced Institute of Science and Technology
1-1 Asahidai, Nomi 923-1292, Japan
E-mail: afsal@jaist.ac.jp
K. Watanabe, T. Taniguchi
National Institute for Materials Science
1-1 Namiki, Tsukuba 305-0044, Japan

The ORCID identification number(s) for the author(s) of this article can be found under https://doi.org/10.1002/apxr.202300064

DOI: 10.1002/apxr.202300064

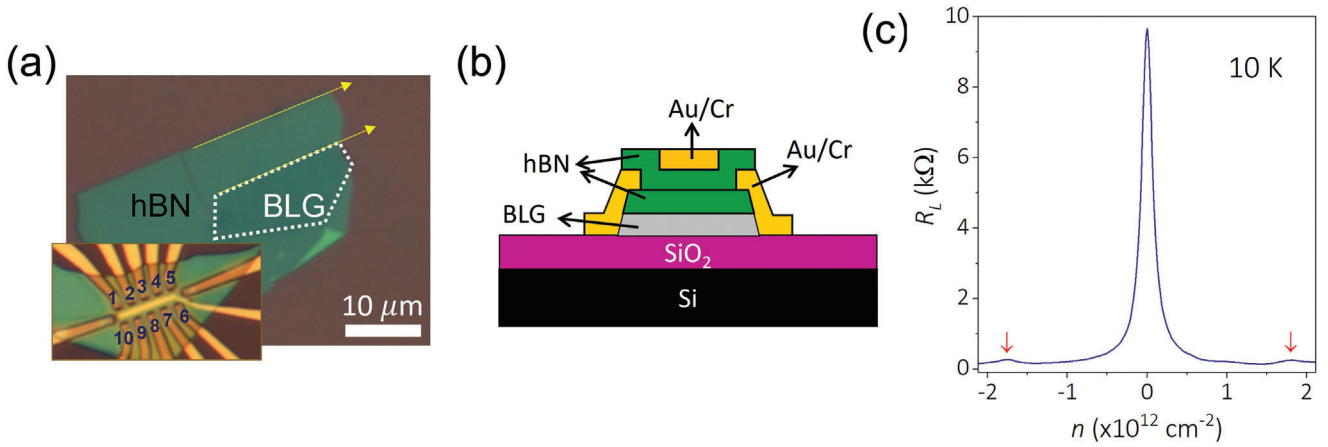

Figure 1. a) Optical image of hBN/bilayer graphene heterostructure aligned with near-zero twist angle. The dotted line shows the graphene region. The arrow indicates the edges of graphene and hBN, which are aligned. The inset shows the optical image of the final device. b) The heterostructure schematic diagram shows the passivation hBN layer and the top gate electrode. C) Measured gate characteristics of the device as a function of carrier density *n*. The arrow indicates the two secondary Dirac peaks at the electron and hole sides. The measurement is performed at 10 K.

and Device B, are fabricated. The results presented in the main text are from Device A (see Supporting Information for the results from Device B). **Figure 1**a shows the optical image of the hBN/bilayer graphene heterostructure from which Device A is fabricated. The dotted line outlines the bilayer graphene area. The bilayer graphene is AB-stacked, and the layer number is confirmed through Raman spectroscopy. The arrows indicate the edges of hBN and bilayer graphene, which are aligned with a near-zero twist angle. After etching the heterostructure into a Hall bar, edge contacts were fabricated.[21] Later a passivation hBN layer is transferred on top of the heterostructure, above which the top gate electrode is fabricated. Figure 1a inset and Figure 1b show the optical image and schematic diagram of the final device. Figure 1c shows the gate characteristics of the device. The field-effect carrier mobility extracted from the linear region around the main Dirac peak (MDP) is ≈ 19 000 $cm^2\ V^{-1}\ s^{-1}$ and ≈ 26 000 $cm^2\ V^{-1}\ s^{-1}$, respectively, for the holes and electrons. Apart from the MDP, secondary Dirac peaks (SDP), which is the signature of the formation of moiré superlattice, can be observed on both sides of the main Dirac peak. The SDP appears at $\pm 1.78 \times 10^{12}\ cm^{-2}$, which corresponds to a moiré superlattice period of 15.3 nm. This period is slightly larger than the maximum period (13.8 nm) expected for an hBN-graphene moiré superlattice. The slight increase in the periodicity is attributed to the stretching of the bilayer graphene (supporting Information II),[5,22,23] which could be originated from the non-uniformity of the SiO_2 substrate.

The local and non-local electrical measurements are performed following the standard four-terminal method using KEITHLEY 4200 semiconductor parameter analyzer with a high input impedance ($10^{13}\ \Omega$) at the voltage terminals. A separate source meter (KEITHLEY 2400) is used to apply gate voltage. **Figure 2**a compares the local (R_L) and non-local (R_{NL}) resistance measurement results for Device A at 10 K. For R_L, a current is applied between terminals two and three, and the voltage drop between terminals nine and eight is detected, giving $R_L = V_{9,8}/I_{2,3}$. For R_{NL} measurement, the current is applied at the local terminals three and eight, and the voltage drop at terminals two and nine is measured, giving $R_{NL} = V_{2,9}/I_{3,8}$. The length and width of the Hall bar in the measured region are 2.5 μm and 1 μm, respectively (A schematic diagram showing the device dimensions in detail is given in the Supporting Information). A strong R_{NL} signal is detected around the charge neutrality point (CNP) with zero electric or magnetic field applied across the layers. The peak of the R_{NL} generally appears at the CNP. The shift in the R_{NL} peak is attributed to the in-homogeneity in the bilayer graphene channel, especially since the graphene is on SiO_2 substrate. To rule out the possibility of diffusive charge contribution to the measured non-local signal, we also calculated the Ohmic contribution using the formula $R_{NL}^{Ohm} = R_L(\frac{W}{\pi L})\exp(-\frac{\pi L}{W})$.[24] The calculated Ohmic contribution is at least one order of magnitude less than that of the measured R_{NL}, thereby ruling out the possibility of diffusive charge contribution. One possible origin of the observed R_{NL} would be the VHE. The Berry curvature induced VHE, and the resultant transverse valley Hall conductivity (σ_{xy}^{VH}) is related to the measured R_{NL} as

$$R_{NL} = \frac{1}{2}\left(\frac{\sigma_{xy}^{VH}}{\sigma_{xx}}\right)^2 \frac{W}{\sigma_{xx} l_v} \exp\left(-\frac{L}{l_v}\right) \quad (1)$$

where L and W are the length and width of the device, l_v is the valley diffusion length and $\sigma_{xx} = 1/\rho$ is the conductivity. Here, ρ is defined as $R_L(W/L)$ where W and L are the width and length of the measured part of the channel, respectively. In the small valley Hall angle regime ($\sigma_{xy}^{VH}/\sigma_{xx}) \ll 1$), R_{NL} and ρ holds a cubic scaling relation ($R_{NL} \propto \rho^3$). Thus we plotted R_{NL} as a function of ρ as shown in Figure 2b, which exhibits a clear cubic relation implying that the measured R_{NL} indeed originates from the VHE. The origin of the VHE can be explained as follows. Aligning hBN with bilayer graphene creates a moiré superlattice with periodic regions where the heterostructure is commensurately stacked.[5,8] Such commensurately stacked regions induce a global asymmetry between the non-dimer atoms (which constitute the low energy bands) in the top and bottom layers, resulting in global layer

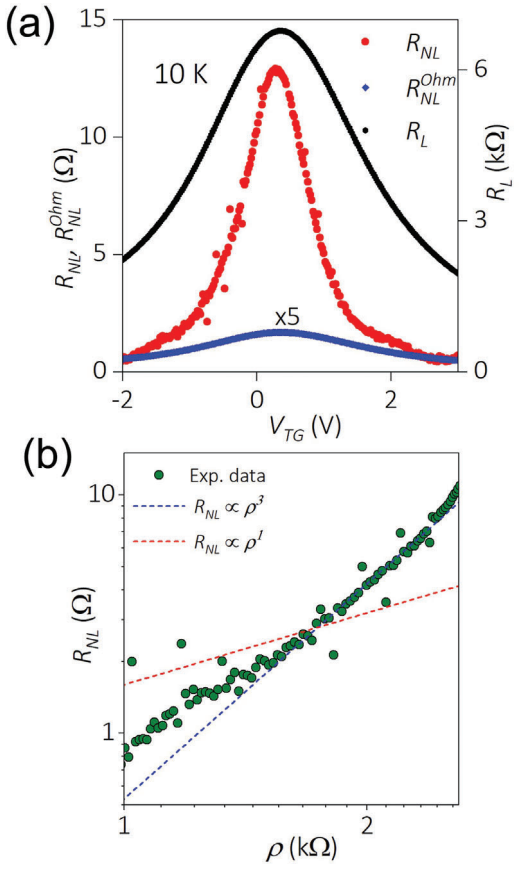

Figure 2. a) Measured local (R_L) and non-local (R_{NL}) resistance for the heterostructure at 10K. The blue line is the calculated Ohmic contribution to the non-local resistance. b) R_{NL} and ρ follows a cubic scaling relation ($R_{NL} \propto \rho^3$) indicating that the measured R_{NL} originates from VHE.

asymmetry. The broken layer symmetry will open a bandgap and induce a finite Berry curvature at the CNP, resulting in VHE.

Next, we investigate the effect of an electric displacement field applied across the bilayer graphene on both R_L and R_{NL}. **Figures 3**a, b show the heat map of the R_L and R_{NL}, respectively, as a function of both top-gate and bottom-gate voltage. It can be seen that the R_{NL} is narrower than $R_{L,}$ indicating the difference in the physical origin of both peaks. Applying voltages on the top and bottom gates allows the independent control of carrier concentration and the displacement field. The displacement fields related to the top and bottom gates (V_{TG} and V_{BG}) are defined as

$$D_{TG} = -\epsilon_{TG}(V_{TG} - V^0_{TG})/d_{TG}$$
$$D_{BG} = -\epsilon_{BG}(V_{BG} - V^0_{BG})/d_{BG} \quad (2)$$

where $\epsilon_{TG}(\epsilon_{BG})$ and $d_{TG}(d_{BG})$ are the dielectric constant and thickness of the top(bottom) layer. $V^0_{TG,BG}$ is the voltage offset, which is -1.2 and 10 V, respectively, for Device A. The difference between the two displacement fields gives the carrier doping, and the average of the two is the net displacement fields. Figure 3c shows the evolution of R_L and R_{NL} as a function of the displacement field. Here R_L and R_{NL} are plotted as a function of top gate voltage with the back gate fixed at different values. As mentioned earlier, the heterostructure at the pristine state ($V_{BG} = 0V$) shows a clear non-local signal, suggesting an in-built asymmetry present in the heterostructure. Application of a negative electric field (V_{BG} = -20 and -10V) increases the intensity of both R_L and R_{NL}. This implies that a negative electric field widens the bandgap and enhances the asymmetry between the layers. Whereas the application of the offset bottom-gate voltage ($V^0_{BG} = 10V$) reduces the intensity of both peaks, suggesting a reduction in the bandgap and the asymmetry. However, the application of a strong positive electric field ($V_{BG} = 30V$) yet again increases the intensity of both R_L and R_{NL}, implying an increase in bandgap and asymmetry of the heterostructure.

To validate the above hypothesis, we measured the temperature dependence of the R_L at different gate voltages to calculate the bandgap. The maximum of the local resistivity (ρ_L^{max}) at the high-temperature regime is related to the bandgap as:

$$\frac{1}{\rho_L^{max}} = \frac{1}{\rho_L}\exp\left(-\frac{E^L}{k_B T}\right) \quad (3)$$

where ρ_L is the local resistivity, E^L is the activation energy, k_B is the Boltzmann constant, and T is the temperature. The bandgap E_g, defined as $2E^L$, can be extracted by plotting $1/\rho_L^{max}$ as a function of $1/T$ as shown in **Figure 4**. The dotted line is the fit to Equation (3) at the high-temperature regime. **Table 1** shows the extracted bandgap values at different V_{BG}. The heterostructure has an intrinsic bandgap of 25 meV (at V_{BG} = 0 V), suggesting that the bandgap originates from the alignment of bilayer graphene with the hBN. Application of a negative displacement field enhances the bandgap (35.3 meV at V_{BG}= -10 V and 45.5 meV at V_{BG}= -20 V). At the same time, the bandgap reduces to a value of 17.5 meV at the offset bottom-gate voltage ($V^0_{BG} = 10V$). This is consistent with the earlier observation of an increase(decrease) in the R_L and R_{NL} peak intensity at the negative(positive) displacement field.

We have also performed ab initio calculations to substantiate the experimental observations (see [25–28] for calculation details). The heterostructure is formed by stacking a unit cell of bilayer graphene on top of an hBN unit cell. The lattice parameter of hBN is matched to that of graphene to create a commensurate stacking to mimic the experimental scenario. **Figure 5**a–e shows the electronic band structure calculated for the hBN/bilayer graphene heterostructure at different electric fields applied across the layers. The heterostructure has an intrinsic bandgap of 36 meV (Figure 5c), implying asymmetry between the layers. As the low energy bands are constituted by the non-dimer atoms in the bottom and top layers of the bilayer graphene, the hBN induces different potentials between them, which opens a bandgap. Applying a negative electric field (Figure 5a,b) introduces additional asymmetry between the layers, enhancing the bandgap (75 meV for -0.25 Vnm^{-1} and 92 meV for -0.5 Vnm^{-1}). However, applying a positive electric field initially works against the inbuilt asymmetry between the layers, reducing the bandgap to 21 meV (Figure 5d). At higher positive electric fields, the electric potential surpasses the intrinsic potential difference between the layers and widens the bandgap further (40 meV for 1.25 Vnm^{-1}), as shown in Figure 5e. The results of the band structure calculation strongly agree with the experimental observa-

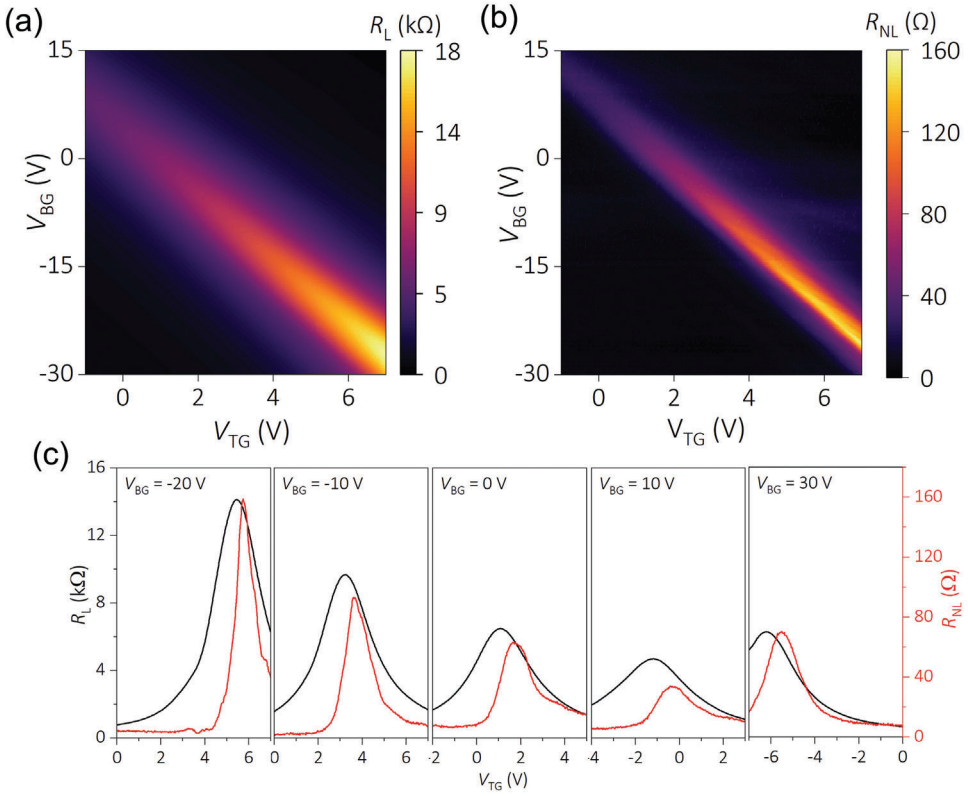

Figure 3. Heat map of the (a) R_L and (b) R_{NL} as a function of top-gate and bottom-gate. c) R_L and R_{NL} measured as a function of top-gate voltage with back-gate fixed at different values. All the measurements are performed at 10 K.

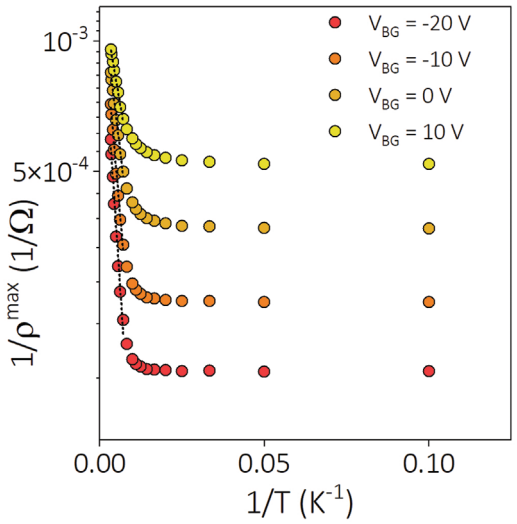

Figure 4. $1/\rho_L^{max}$ as a function of $1/T$ plot for different V_{BG} showing the temperature dependence of ρ_L^{max}. The dotted line indicates the fitting to Equation (3) in the high-temperature regime from which the bandgap of the heterostructure at different V_{BG} is extracted.

tions. Next, we look at the Berry curvature calculated for the heterostructure. Berry curvature for an electronic band is defined as

$$\mathbf{\Omega}_n(\mathbf{k}) = i\frac{\hbar^2}{m^2}\sum_{n\neq n'}\frac{\langle u_{n,\mathbf{k}}|\hat{\mathbf{p}}|u_{n',\mathbf{k}}\rangle \times \langle u_{n',\mathbf{k}}|\hat{\mathbf{p}}|u_{n,\mathbf{k}}\rangle}{(\epsilon_n - \epsilon_{n'})^2} \quad (4)$$

Table 1. Bandgap extracted from the $1/\rho_L^{max}$ versus $1/T$ plot for different V_{BG}. $E_\perp$ is the electric field corresponding to each V_{BG} at ρ_L^{max}.

V_{BG} (V)	$E_\perp$ (V/nm)	Band gap (meV)	R_{NL}^{max} (Ω)
-20	-0.44	45.5	160
-10	-0.30	35.3	94
0	-0.14	24.8	64
10	0.00	17.5	34

where $|u_{n,k}\rangle$ is the periodic part of the Bloch function, $\hat{\mathbf{p}}$ is the momentum operator, ϵ_n is the energy of the nth band and $\epsilon_{n'}$ represents the energy of all other bands. The total Berry curvature is the sum of the individual occupied band's Berry curvature ($\mathbf{\Omega}(\mathbf{k}) = \sum_n f_n \mathbf{\Omega}_n(\mathbf{k})$). The Wannier interpolation scheme dictates that a pair of bands that are either occupied or unoccupied have a negligible contribution to the total Berry curvature.[29] The major contribution to the total Berry curvature comes from a pair of bands where one is occupied and another unoccupied, such as the low energy bands in the hBN/bilayer graphene heterostructure. In addition, the denominator of Equation (4) suggests that the Berry curvature value varies as the square of the energy difference between two adjacent bands. Thus in our case, the Berry curvature changes with the electric field as the band gap changes. The heterostructure has an intrinsic non-zero Berry curvature, as shown in Figure 5h. A negative electric field reduces the magnitude of the Berry curvature as it widens the gap between the low

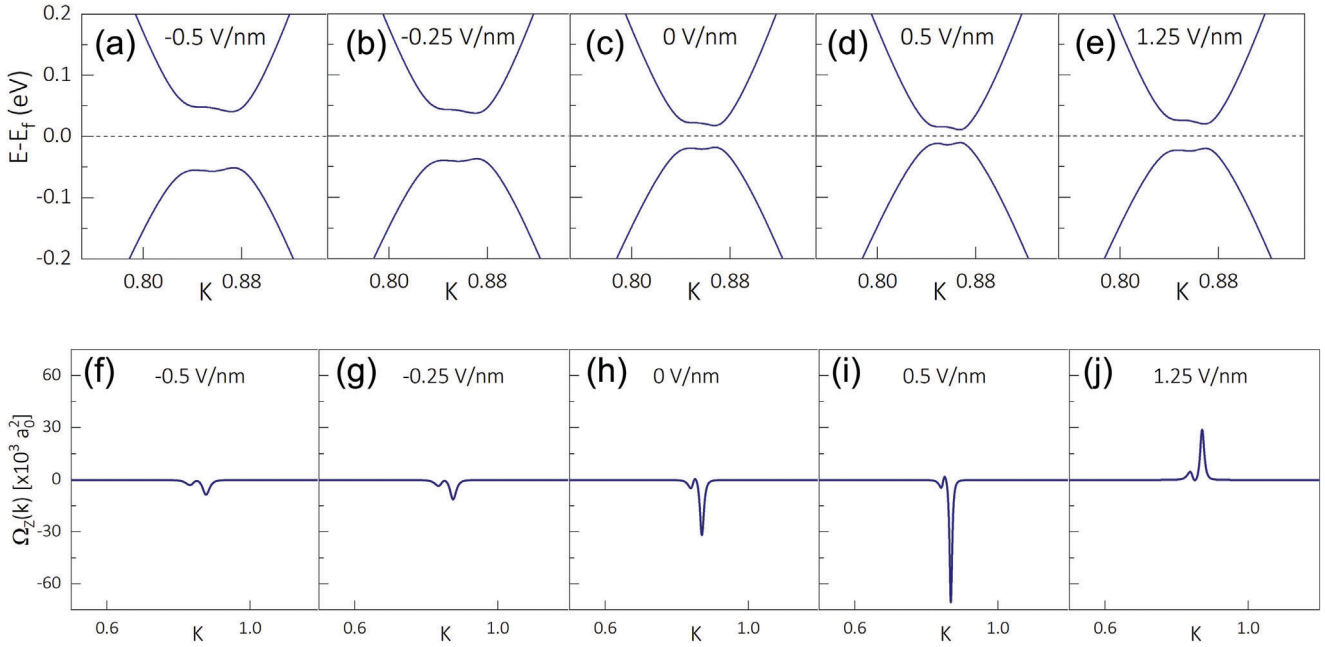

Figure 5. Electronic band structure calculated for the hBN/bilayer graphene heterostructure at electric fields of magnitude a) -0.5 Vnm^{-1}, b) -0.25 Vnm^{-1}, c) 0 Vnm^{-1}, d) 0.5 Vnm^{-1}, and e) 1.25 Vnm^{-1}. The path of the band structure calculation is $M \rightarrow K \rightarrow \Gamma$. Berry curvature calculated at K high symmetry point for the heterostructure at electric fields of magnitude f) -0.5 Vnm^{-1}, g) -0.25 Vnm^{-1}, h) 0 Vnm^{-1}, i) 0.5 Vnm^{-1}, and j) 1.25 Vnm^{-1}. The path of the Berry curvature calculation is the same as the band structure calculation.

energy bands (Figure 5f,g). On the other hand, a small positive electric field (0.5 Vnm^{-1}) enhances the magnitude of the Berry curvature due to the narrow bandgap (Figure 5i). However, two key differences could be observed at a higher positive electric field (Figure 5j). One, the magnitude of the Berry curvature reduces owing to the widening of the bandgap. The second is the change in the polarity of the Berry curvature, which implies that the polarity of the layer asymmetry switches direction at higher positive electric fields.

3. Conclusion

In conclusion, we have observed Berry curvature induced VHE in non-encapsulated hBN/bilayer graphene heterostructure, where the hBN and bilayer graphene are aligned with a near-zero twist angle. Aligning bilayer graphene with hBN gives rise to a global bandgap and a finite Berry curvature at the CNP, resulting in VHE. The VHE is detected as a non-local resistance near the CNP. The cubic relation observed between R_{NL} and ρ validates that the measured R_{NL} indeed originates from the VHE. The measured R_{NL} could be manipulated with the application of a displacement field across the layers, which is attributed to the change in the electronic band structure and the asymmetry of the bilayer graphene under a displacement field. The intrinsic bandgap of the heterostructure and its evolution under the displacement field is confirmed from the temperature-dependent R_L measurement in the high-temperature regime. The experimental observations were substantiated with ab initio calculations that showed that the heterostructure has an intrinsic bandgap and a non-zero Berry curvature, both of which could be controlled by a perpendicular electric field.

Supporting Information

Supporting Information is available from the Wiley Online Library or from the author.

Acknowledgements

T.S. and A.K. contributed equally to this work. Part of this research was supported by Toshiba electronic devices and storage corporation's academic encouragement program.

Conflict of Interest

The authors declare no conflict of interest.

Data Availability Statement

The data that support the findings of this study are available from the corresponding author upon reasonable request.

Keywords

bilayer graphene, hBN, valleytronics

Received: June 5, 2023
Revised: July 28, 2023
Published online: August 31, 2023

[1] J. R. Schaibley, H. Yu, G. Clark, P. Rivera, J. S. Ross, K. L. Seyler, W. Yao, X. Xu, *Nat. Rev. Mater.* **2016**, *1*, 16055.

[2] S. A. Vitale, D. Nezich, J. O. Varghese, P. Kim, N. Gedik, P. Jarillo-Herrero, D. Xiao, M. Rothschild, *Small* **2018**, *14*, 1801483.
[3] X. Xu, W. Yao, D. Xiao, T. F. Heinz, *Nat. Phys.* **2014**, *10*, 343.
[4] M. Yankowitz, J. Xue, D. Cormode, J. D. Sanchez-Yamagishi, K. Watanabe, T. Taniguchi, P. Jarillo-Herrero, P. Jacquod, B. J. LeRoy, *Nat. Phys.* **2012**, *8*, 382.
[5] C. R. Woods, L. Britnell, A. Eckmann, R. S. Ma, J. C. Lu, H. M. Guo, X. Lin, G. L. Yu, Y. Cao, R. V. Gorbachev, A. V. Kretinin, J. Park, L. A. Ponomarenko, M. I. Katsnelson, Yu. N. Gornostyrev, K. Watanabe, T. Taniguchi, C. Casiraghi, H-J. Gao, A. K. Geim, K. S. Novoselov, *Nat. Phys.* **2014**, *10*, 451.
[6] J. C. W. Song, P. Samutpraphoot, L. S. Levitov, *PNAS* **2015**, *112*, 10879.
[7] M. Yankowitz, Q. Ma, P. Jarillo-Herrero, B. J. LeRoy, *Nat. Rev. Phys.* **2019**, *1*, 112.
[8] R. V. Gorbachev, J. C. W. Song, G. L. Yu, A. V. Kretinin, F. Withers, Y. Cao, A. Mishchenko, I. V. Grigorieva, K. S. Novoselov, L. S. Levitov, A. K. Geim, *Science* **2014**, *346*, 448.
[9] K. Komatsu, Y. Morita, E. Watanabe, D. Tsuya, K. Watanabe, T. Taniguchi, S. Moriyama, *Sci. Adv.* **2018**, *4*, eaaq0194.
[10] Y. Li, M. Amado, T. Hyart, G. P. Mazur, J. W. A. Robinson, *Commun. Phys.* **2020**, *3*, 224.
[11] E. McCann, *Phys. Rev. B* **2006**, *74*, 161403(R).
[12] H. Min, B. Sahu, S. K. Banerjee, A. H. MacDonald, *Phys. Rev. B* **2007**, *75*, 155115.
[13] J. B. Oostinga, H. B. Heersche, X. Liu, A. F. Morpurgo, L. M. K. Vandersypen, *Nat. Mater.* **2007**, *7*, 151.
[14] Y. Zhang, T.-T. Tang, C. Girit, Z. Hao, M. C. Martin, A. Zettl, M. F. Crommie, Y. R. Shen, F. Wang, *Nature* **2009**, *459*, 820.
[15] C. R. Dean, L. Wang, P. Maher, C. Forsythe, F. Ghahari, Y. Gao, J. Katoch, M. Ishigami, P. Moon, M. Koshino, T. Taniguchi, K. Watanabe, K. L. Shepard, J. Hone, P. Kim, *Nature* **2013**, *497*, 598.
[16] M. Sui, G. Chen, L. Ma, W.-Y. Shan, D. Tian, K. Watanabe, T. Taniguchi, X. Jin, W. Yao, D. Xiao, Y. Zhang, *Nat. Phys.* **2015**, *11*, 1027.
[17] Y. Shimazaki, M. Yamamoto, I. V. Borzenets, K. Watanabe, T. Taniguchi, S. Tarucha, *Nat. Phys.* **2015**, *11*, 1032.
[18] K. Endo, K. Komatsu, T. Iwasaki, E. Watanabe, D. Tsuya, K. Watanabe, T. Taniguchi, Y. Noguchi, Y. Wakayama, Y. Morita, S. Moriyama, *Appl. Phys. Lett.* **2019**, *114*, 243105.
[19] E. Arrighi, V.-H. Nguyen, M. Di Luca, G. Maffione, K. Watanabe, T. Taniguchi, D. Mailly, J.-C. Charlier, R. Ribeiro-Palau, Non-identical moiré twins in bilayer graphene, arXiv:2205.01760v2.
[20] A. Kareekunnan, M. Muruganathan, H. Mizuta, *Phys. Rev. B* **2020**, *101*, 195406.
[21] L. Wang, I. Meric, P. Y. Huang, Q. Gao, Y. Gao, H. Tran, T. Taniguchi, K. Watanabe, L. M. Campos, D. A. Muller, J. Guo, P. Kim, J. Hone, K. L. Shepard, C. R. Dean, *Science* **2013**, *342*, 614.
[22] Z. Wang, Y. B. Wang, J. Yin, E. Tóvári, Y. Yang, L. Lin, M. Holwill, J. Birkbeck, D. J. Perello, S. Xu, J. Zultak, R. V. Gorbachev, A. V. Kretinin, T. Taniguchi, K. Watanabe, S. V. Morozov, M. Andelković, S. P. Milovanovic, L. Covaci, F. M. Peeters, A. Mishchenko, A. K. Geim, K. S. Novoselov, V. I. Fal'ko, A. Knothe, C. R. Woods, *Sci. Adv.* **2019**, *5*, eaay8897.
[23] X. Sun, S. Zhang, Z. Liu, H. Zhu, J. Huang, K. Yuan, Z. Wang, K. Watanabe, T. Taniguchi, X. Li, M. Zhu, J. Mao, T. Yang, J. Kang, J. Liu, Y. Ye, Z. V. Han, Z. Zhang, *Nat. Commun.* **2021**, *12*, 7196.
[24] D. A. Abanin, S. V. Morozov, L. A. Ponomarenko, R. V. Gorbachev, A. S. Mayorov, M. I. Katsnelson, K. Watanabe, T. Taniguchi, K. S. Novoselov, L. S. Levitov, A. K. Geim, *Science* **2011**, *332*, 328.
[25] The ab initio calculations are performed using the SIESTA package, which uses the linear combination of atomic orbitals (LCAO) basis sets.[26] To maintain similar interlayer distance between the layers as the experimental values, van der Waals exchange-correlation functionals were used.[27] A vacuum layer of 25 Åwas used to reduce the interaction between adjacent structures. For all the calculations, a Monkhorst-Pack grid of $40 \times 40 \times 1$ and an energy cutoff of 500 Ry were used. Structure optimization was performed until the force between atoms was less than 0.01 eV/Å. The Berry curvature calculation was performed using the WANNIER90 package.[28] A total of 15 Wannier functions were used on a Monkhorst-Pack grid of $40 \times 40 \times 1$ to calculate the Berry curvature.
[26] J. Soler, E. Artacho, J. D. Gale, A. García, J. Junquera, P. Ordejón, D. Sánchez-Portal, *J. Phys.: Condens. Matter* **2002**, *14*, 2745.
[27] M. Dion, H. Rydberg, E. Schröder, D. C. Langreth, B. I. Lundqvist, *Phys. Rev. Lett.* **2004**, *92*, 246401.
[28] G. Pizzi, V. Vitale, R. Arita, S. Blügel, F. Freimuth, G. Géranton, M. Gibertini, D. Gresch, C. Johnson, T. Koretsune, J. Ibañez-Azpiroz, H. Lee, J.-M. Lihm, D. Marchand, A. Marrazzo, Y. Mokrousov, J. I. Mustafa, Y. Nohara, Y. Nomura, L. Paulatto, S. Poncé, T. Ponweiser, J. Qiao, F. Thöle, S. S. Tsirkin, M. Wierzbowska, N. Marzari, D. Vanderbilt, I. Souza, A. A. Mostofi, et. al.,*J. Phys.: Condens. Matter* **2020**, *32*, 165902.
[29] X. Wang, J. R. Yates, I. Souza, D. Vanderbilt, *Phys. Rev. B* **2006**, *74*, 195118.